

# Mass and density of the transiting hot and rocky super-Earth LHS 1478 b (TOI-1640 b)

M. G. Soto<sup>1</sup>, G. Anglada-Escudé<sup>1,2,3</sup>, S. Dreizler<sup>4</sup>, K. Molaverdikhani<sup>5,6</sup>, J. Kemmer<sup>5</sup>, C. Rodríguez-López<sup>7</sup>, J. Lillo-Box<sup>8</sup>, E. Pallé<sup>9,10</sup>, N. Espinoza<sup>11</sup>, J. A. Caballero<sup>8</sup>, A. Quirrenbach<sup>5</sup>, I. Ribas<sup>2,3</sup>, A. Reiners<sup>4</sup>, N. Narita<sup>12,13,14,9</sup>, T. Hirano<sup>15,14,16</sup>, P. J. Amado<sup>7</sup>, V. J. S. Béjar<sup>9,10</sup>, P. Bluhm<sup>5</sup>, C. J. Burke<sup>26</sup>, D. A. Caldwell<sup>17,18</sup>, D. Charbonneau<sup>19</sup>, R. Cloutier<sup>19</sup>, K. A. Collins<sup>19</sup>, M. Cortés-Contreras<sup>8</sup>, E. Girardin<sup>20</sup>, P. Guerra<sup>21</sup>, H. Harakawa<sup>22</sup>, A. P. Hatzes<sup>23</sup>, J. Irwin<sup>19</sup>, J. M. Jenkins<sup>18</sup>, E. Jensen<sup>24</sup>, K. Kawauchi<sup>15</sup>, T. Kotani<sup>14,16,25</sup>, T. Kudo<sup>22</sup>, M. Kunitomo<sup>26</sup>, M. Kuzuhara<sup>14,16</sup>, D. W. Latham<sup>19</sup>, D. Montes<sup>27</sup>, J. C. Morales<sup>2,3</sup>, M. Mori<sup>28</sup>, R. P. Nelson<sup>1</sup>, M. Omiya<sup>14,16</sup>, S. Pedraz<sup>29</sup>, V. M. Passegger<sup>30,31</sup>, B. V. Rackham<sup>32</sup>, A. Rudat<sup>26</sup>, J. E. Schlieder<sup>33</sup>, P. Schöfer<sup>4</sup>, A. Schweitzer<sup>30</sup>, A. Selezneva<sup>21</sup>, C. Stockdale<sup>34</sup>, M. Tamura<sup>28,14,16</sup>, T. Trifonov<sup>6</sup>, R. Vanderspek<sup>26</sup>, and D. Watanabe<sup>35</sup>

(Affiliations can be found after the references)

Received 19 February 2021 / Accepted 29 March 2021

## ABSTRACT

One of the main objectives of the Transiting Exoplanet Survey Satellite (TESS) mission is the discovery of small rocky planets around relatively bright nearby stars. Here, we report the discovery and characterization of the transiting super-Earth planet orbiting LHS 1478 (TOI-1640). The star is an inactive red dwarf ( $J \sim 9.6$  mag and spectral type m3 V) with mass and radius estimates of  $0.20 \pm 0.01 M_{\odot}$  and  $0.25 \pm 0.01 R_{\odot}$ , respectively, and an effective temperature of  $3381 \pm 54$  K. It was observed by TESS in four sectors. These data revealed a transit-like feature with a period of 1.949 days. We combined the TESS data with three ground-based transit measurements, 57 radial velocity (RV) measurements from CARMENES, and 13 RV measurements from IRD, determining that the signal is produced by a planet with a mass of  $2.33^{+0.20}_{-0.20} M_{\oplus}$  and a radius of  $1.24^{+0.05}_{-0.05} R_{\oplus}$ . The resulting bulk density of this planet is  $6.67 \text{ g cm}^{-3}$ , which is consistent with a rocky planet with an Fe- and MgSiO<sub>3</sub>-dominated composition. Although the planet would be too hot to sustain liquid water on its surface (its equilibrium temperature is about  $\sim 595$  K, suggesting a Venus-like atmosphere), spectroscopic metrics based on the capabilities of the forthcoming *James Webb* Space Telescope and the fact that the host star is rather inactive indicate that this is one of the most favorable known rocky exoplanets for atmospheric characterization.

**Key words.** planets and satellites: detection – planets and satellites: fundamental parameters – techniques: photometric – techniques: radial velocities

## 1. Introduction

Stars smaller than the Sun offer a number of advantages as to the detection of exoplanets with both the Doppler (e.g., Proxima b; Anglada-Escudé et al. 2016) and photometric transit methods (e.g., the TRAPPIST-1 system; Gillon et al. 2017). Both are indirect methods that rely on the planet imprinting a signal onto the star light. The Doppler technique measures the radial velocity (RV) of the star by measuring to high accuracy the wavelength shift of numerous absorption features in the stellar spectrum. The amplitude of the signal is larger for a larger planet-star mass ratio and for shorter orbital periods. The transit method relies on measuring the light blocked by the planet as it crosses the stellar disk. In this case, the signal is proportional to the planet-star area ratio, and it repeats once per orbital period. With both methods, shorter-period planets are, therefore, more easily detectable.

Exoplanet surveys with the Doppler technique are typically conducted with ground-based high-resolution spectrometers ( $R = \lambda/\delta\lambda > 50\,000$ ) that are kept in a very stable environment and are calibrated against spectral features of a reference source measured in the laboratory. This is the case for the CARMENES spectrometer (Quirrenbach et al. 2016), which was specifically designed to obtain maximal precision on

red dwarf stars. The CARMENES survey has led to numerous new exoplanet discoveries in the super-Earth to Earth-mass regime, in hot to warm temperate orbits (e.g., Luque et al. 2018; Zechmeister et al. 2019; Stock et al. 2020). Several of these planets have been detected both in transit and by RV (Luque et al. 2019; Dreizler et al. 2020; Kemmer et al. 2020; Nowak et al. 2020; Bluhm et al. 2020). On the other hand, the NASA Transiting Exoplanet Survey Satellite (TESS) mission (Ricker et al. 2015) has been surveying most of the sky for signals of transiting planets, with the goal of detecting those that should enable a more straightforward atmospheric characterization. To date, TESS has revealed numerous exoplanet candidates that are transiting nearby M dwarfs (Astudillo-Defru et al. 2020; Gan et al. 2020; Kanodia et al. 2020; Trifonov et al. 2021, to name a few).

One key element in the characterization and study of transiting planets is their confirmation using Doppler spectroscopy, which in turn produces a measurement of their masses, allowing one to derive their mean bulk densities and put constraints on their compositions. Finally, the atmospheres of transiting planets can be studied by performing spectroscopic measurements during transits (the planet blocks more light at certain wavelengths where the molecules in its atmosphere deter more light, producing deeper transits) and secondary eclipses (the spectrum

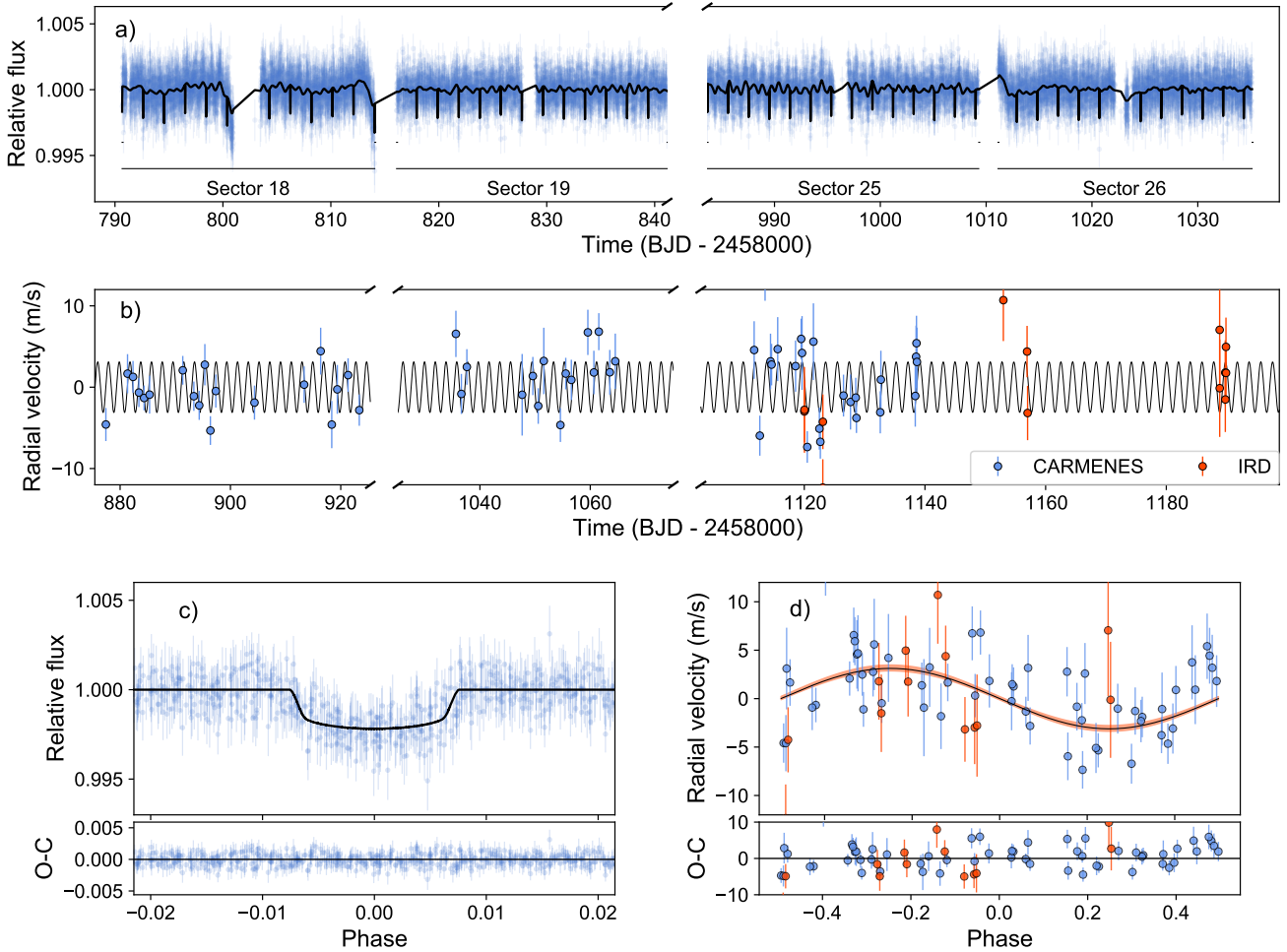


**Fig. 1.** Data and joint fit results of LHS 1478 with *juliet* (Sect. 3.2). *Top (a)*: TESS photometry, with the black line representing the best transit+GP fit. *Middle (b)*: RV data from CARMENES and IRD, with the jitter term added to the uncertainties. The black line is the best fit Keplerian model. *Bottom left (c)*: phased-folded TESS data, with the GP component removed. The black line is the best transit fit. The *bottom sub-panel* shows the residuals from the transit fit. *Bottom right (d)*: phased-folded RV data. The black line is the best fit Keplerian model, and the red shaded area represents the 68% CI. *Bottom sub-panel*: residuals after removing the Keplerian fit.

of thermal emission of the planet is also affected by the presence of absorbing molecules, producing a shallower dip in the light curve when the planet goes behind the star). Among these, and thanks to the more favorable radius ratio between the planet and the star, exoplanets transiting red dwarfs are the best ones for atmospheric characterization. The measured spectrum of an exoplanet can be affected by the presence of spots and active regions in the visible part of the star during transits (Rackham et al. 2018): the less active the star is, the cleaner and easier it is to interpret the measured spectrum of a planet. Due to its properties (transiting, Doppler signal in the few  $\text{m s}^{-1}$  regime) and its host star (small, relatively nearby, and low stellar activity), LHS 1478 b satisfies all the favorable conditions for becoming a prime target for the characterization of rocky terrestrial planets.

In this paper, we validate the transiting exoplanet LHS 1478 b (TOI-1640 b). We provide an overview of the measurements with photometry (initial detection, stellar activity, orbital period, and planet size), imaging (validation against false positives), and RV (confirmation, stellar activity, and measurement of the planet mass) in Sect. 2. Stellar parameters are presented in Sect. 3.1, and a joint analysis to constrain the planet properties is given in Sect. 3.2. We discuss the results in the context of terrestrial planet candidates and further follow-up in Sect. 4 and summarize our work in Sect. 5.

## 2. Data

### 2.1. TESS photometry

LHS 1478 (TOI-1640) was observed by TESS in sectors 18, 19, 25, and 26 of its primary mission. The data were processed through the Science Processing Operations Center (SPOC; Jenkins et al. 2016), and transiting planet search algorithms (Jenkins 2002; Jenkins et al. 2010) detected a signal with a period of  $1.949521 \pm 0.000007$  d and a transit depth of  $2185 \pm 111$  parts-per-million (ppm) in December 2019 based on the data from sector 18. After reviewing the results of the data validation reports (Twicken et al. 2018; Li et al. 2019), the TESS Science Office alerted the community of TOI-1640 on 14 January 2020<sup>1</sup>.

We obtained the photometric light curve, corrected for systematics (Presearch Data Conditioning, or PDC; Smith et al. 2012), from the Mikulski Archive for Space Telescopes<sup>2</sup> (MAST) using the *lightkurve*<sup>3</sup> package (Lightkurve Collaboration 2018). The data are shown in Fig. 1. We performed a period search using the Box-Fitting Least Squares (BLS; Kovács et al. 2002) and the Transit Least Squares (TLS;

<sup>1</sup> <https://tess.mit.edu/toi-releases/>

<sup>2</sup> <https://archive.stsci.edu>

<sup>3</sup> <https://github.com/KeplerGO/Lightkurve>

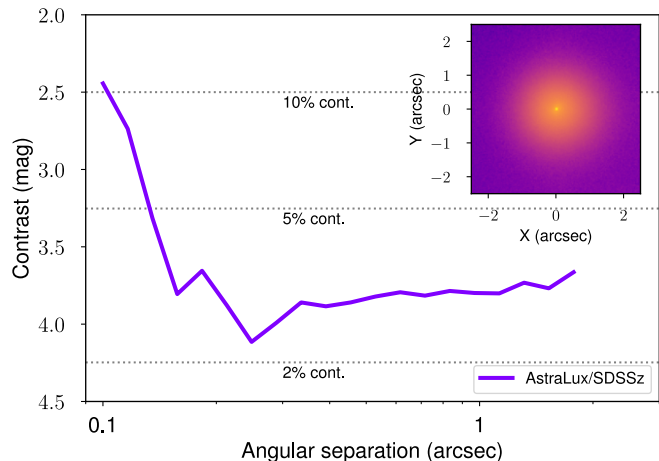
Hippke & Heller 2019) algorithms (Fig. A.1), and we detected with both of them a signal with a period of 1.949 d and a signal detection efficiency (SDE)  $>8$  (empirical transit detection threshold from Aigrain et al. 2016). This period is the same as the one reported by the TESS SPOC.

Figure A.2 shows the TESS field of view and aperture size used for each of the four sectors for LHS 1478, generated using `tpfplotter`<sup>4</sup> (Aller et al. 2020). No sources contaminating the TESS aperture were found in the *Gaia* Early Data Release 3 (EDR3) catalog (Gaia Collaboration 2021) down to a magnitude contrast limit of 6 mag compared to our target. Additionally, the *Gaia* EDR3 renormalized unit weight error (RUWE) value for this target is 1.26, below the critical value of 1.40, which is an indicator that a source is non-single or has a problematic astrometric solution (Lindgren et al. 2021).

## 2.2. High-spatial-resolution imaging

In order to exclude the presence of contaminants close to our target, we observed LHS 1478 with the AstraLux high-spatial-resolution camera (Hormuth et al. 2008), located at the 2.2 m telescope of the Calar Alto Observatory (Almería, Spain). This instrument uses the lucky-imaging technique to obtain diffraction-limited images by obtaining thousands of short-exposure frames (below the atmospheric coherence time) to subsequently select those with the highest Strehl ratios (Strehl 1902) and combine them into a final high-spatial-resolution image. We observed this target on the night of 25 February 2020 under good weather conditions with a mean seeing of 1.0 arcsec. We obtained 41 710 frames with 20 ms exposure times for a total exposure of 83.4 s in the Sloan Digital Sky Survey  $z'$  filter (“SDSSz”), with a field of view windowed to  $6 \times 6$  arcsec. The data cube was reduced by the instrument pipeline (Hormuth et al. 2008), and we selected the 10% of frames with the highest quality to produce the final high-resolution image. In order to obtain the sensitivity limits of the image, we used the `astrasens` package<sup>5</sup> with the procedure described in Lillo-Box et al. (2012, 2014). Both the  $5\sigma$  sensitivity curve and the image are shown in Fig. 2. We could exclude sources down to 0.2 arcsec with a magnitude contrast of  $\Delta z' < 4$  mmag, corresponding to a maximum contamination level of 2.5%.

We additionally estimated the probability of an undetected blended source in our high-spatial-resolution image, called the blended source confidence (BSC), following the steps in Lillo-Box et al. (2014). In short, we used a python implementation of this approach (`bsc`), which uses the TRILEGAL<sup>6</sup> galactic model (v1.6; Girardi et al. 2012) to retrieve a simulated source population of the region around the corresponding target<sup>7</sup>. This simulated population was used to compute the density of stars around the target position (radius  $\rho = 1$  deg) and derive the probability of chance alignment at a given contrast magnitude and separation. We applied this to the position of LHS 1478 and used a maximum contrast magnitude of  $\Delta m_{b,\max} = 6.7$  mag in the  $z'$  passband, corresponding to the maximum contrast of a blended eclipsing binary that could mimic the observed transit depth. Using our high-resolution image, we estimated the probability of an undetected blended source to be 0.2%. The probability of such an undetected source being an appropriate eclipsing binary



**Fig. 2.** AstraLux  $5\sigma$  sensitivity curve (main panel) of the high-spatial-resolution image obtained for LHS 1478 (inset) in the SDSSz photometric band.

is even lower, and thus we concluded that the transit signal is not due to a blended eclipsing binary.

## 2.3. Ground-based photometry

Ground-based transit photometry was obtained to confirm the TESS transit event and to refine the ephemeris of the planet. We used the TESS Transit Finder, a customized version of the `Tapir` software package (Jensen 2013), to schedule our observations based on the preliminary ephemeris from the SPOC light curve. We obtained a total of three transit detections, which we included in our joint fit. The individual observations are described below.

### 2.3.1. MEarth-North

LHS 1478 was first observed by the MEarth-North telescope array on 14 January 2020. MEarth-North is located at the Fred Lawrence Whipple Observatory on Mount Hopkins, Arizona, and consists of eight 40 cm telescopes equipped with Apogee U42 cameras and custom RG715 passbands. We reduced the MEarth photometry following the standard procedures outlined by Irwin et al. (2007) and Berta et al. (2012) and using a 6 arcsec aperture.

LHS 1478 was observed continuously with all eight telescopes from an airmass of 1.4–2.0 with 14-s exposures. The observations were taken through intermittent clouds and produced a tentative transit detection amid large residual systematics with a photometric dispersion of 4.2 parts-per-thousand (ppt). Although the combined light curve of the star from all eight telescopes did not yield a reliable transit detection, these data were still used to rule out nearby eclipsing binaries in 101 of 103 sources within 2.5 arcmin and down to a differential magnitude of 8.6 mag. The two uncleared sources are faint ( $\Delta m = 3.8$ –4.0 mag) and are blended with nearby sources. Their wide separations from LHS 1478 (1.8–2.2 arcmin) also make them improbable sources of the TESS transit events.

### 2.3.2. RCO

The first reliable ground-based detection of a transit of LHS 1478 was obtained on 31 January 2020 using the Ritchey-Chrétien Optical (RCO) 40 cm telescope located at the Grand-Pra Observatory near Valais Sion, Switzerland. We observed a full transit in the Sloan  $i'$  passband with an exposure time of 45 s. We used

<sup>4</sup> <https://github.com/jlillo/tpfplotter>

<sup>5</sup> <https://github.com/jlillo/astrasens>

<sup>6</sup> <http://stev.oapd.inaf.it/cgi-bin/trilegal>

<sup>7</sup> This is done in python by using the `astrobase` implementation by Bhatti et al. (2020).

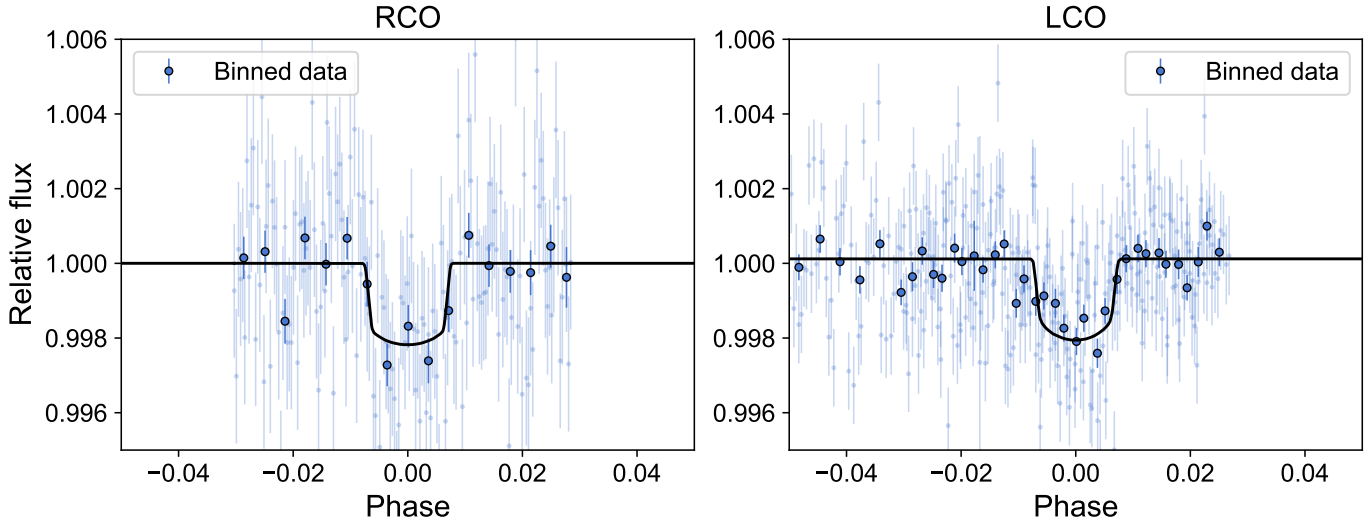


**Fig. 3.** Phased-folded RCO (*left*) and LCOGT (*right*) data. The black line represents the best transit model from *juliet*. The small points show the raw data, while the large points show the data binned into ten-minute bins.

the *AstroImageJ* software package (Collins et al. 2017) to perform differential photometry using 5.1 arcsec apertures and to detrend against airmass in order to produce the light curve of LHS 1478 depicted in the left panel of Fig. 3. With our reduction, we achieved a photometric precision of 1.1 ppt in three-minute bins. We detected the transit of LHS 1478 with a mid-transit time of  $\approx 8$  min late relative to the SPOC prediction (the transit epoch was derived at the time using TESS data from sectors 18 and 19).

### 2.3.3. LCOGT

We observed two additional full transits of LHS 1478 on 27 August 2020 and 7 October 2020 from the Las Cumbres Observatory Global Telescope (LCOGT; Brown et al. 2013) 1.0 m network node at McDonald Observatory. The images were calibrated by the standard LCOGT Banzai pipeline (McCully et al. 2018).

Both light curves were obtained in the Pan-STARRS  $z$ -short passband with exposure times of 40 and 50 s in the August and October runs, respectively. We used *AstroImageJ* to perform differential photometry using 5.8 arcsec apertures and to detrend against airmass. The resulting combined and phase-folded light curves are included in the right panel of Fig. 3. With our reduction, we achieve photometric precisions of 0.7 ppt and 0.5 ppt in three-minute bins, which resulted in a high signal-to-noise ratio (S/N) transit detection in each LCOGT light curve. Both LCOGT transit detections were at the time predicted by the refined ephemeris of LHS 1478 from the RCO detection.

## 2.4. Spectroscopy

### 2.4.1. CARMENES

We obtained a total of 57 spectra of LHS 1478 with CARMENES between 28 January 2020 and 16 October 2020, all taken with exposure times of 1800 s. The visual channel (VIS) of CARMENES has a resolving power  $R = 94\,600$  and covers the spectral range from 520 to 960 nm. Simultaneous wavelength calibration is performed with Fabry-Pérot etalon exposures, which are also used to track the instrument drift at night. The obtained spectra have a median S/N of  $\sim 48$  per pixel at 746 nm. The spectra were reduced with *caracal* Zechmeister et al. 2014;

Caballero et al. 2016b, and the corresponding RVs were extracted using *serval* (Zechmeister et al. 2018) along with selected activity indicators (Sect. 3.1). The RVs were corrected for barycentric motion, instrumental drift, secular acceleration, and nightly zero points (Tal-Or et al. 2019; Trifonov et al. 2020). The root-mean-square uncertainty (rms) and median uncertainty ( $\hat{\sigma}$ ) of the VIS RVs were 4.02 and 2.49  $\text{m s}^{-1}$ , respectively, and are shown in Fig. 1 and Table A.1. A generalized Lomb-Scargle (GLS) periodogram (Zechmeister & Kürster 2009) of the RV data shows a period at 1.949 d, which is consistent with the transit signal, with a theoretically computed false-alarm probability (FAP) of less than 1% (Fig. 4).

The RVs measured with the CARMENES near-infrared (NIR) channel have rms and median uncertainties of 19.26  $\text{m s}^{-1}$  and 9.97  $\text{m s}^{-1}$ , respectively. We excluded the NIR RVs from the analysis because their scatter is higher than the expected planetary amplitude.

### 2.4.2. IRD spectroscopy

We observed LHS 1478 using the InfraRed Doppler (IRD) instrument at the Subaru 8.2 m telescope (Tamura et al. 2012; Kotani et al. 2018) between September and December 2020. A total of 13 spectra were obtained, with an integration time of 900 s. The IRD instrument is a fiber-fed spectrograph that covers the spectral range from 930 to 1740 nm at a resolving power of  $R \sim 70\,000$ . Simultaneous wavelength calibration is performed by injecting light from a laser-frequency comb into the second fiber. The raw data were reduced into one-dimensional spectra using the IRAF software, as well as with a custom code (Kuzuhara et al. 2018; Hirano et al. 2020) to suppress the bias and correlated noise of the detectors. The typical S/N of the reduced spectra ranged from 60 to 95 per pixel at 1000 nm.

Following Hirano et al. (2020), we analyzed the observed spectra to extract precise RVs. In doing so, we combined multiple frames to obtain a high S/N template for the RV analysis, after removing the telluric lines and the instrumental profile of the spectrograph. The relative RV was then measured with respect to this template for each spectrum. The resulting relative RVs after the correction for the barycentric motion of Earth are listed in Table A.2 and shown in Fig. 1. The internal RV error was typically 3–6  $\text{m s}^{-1}$  for each frame.

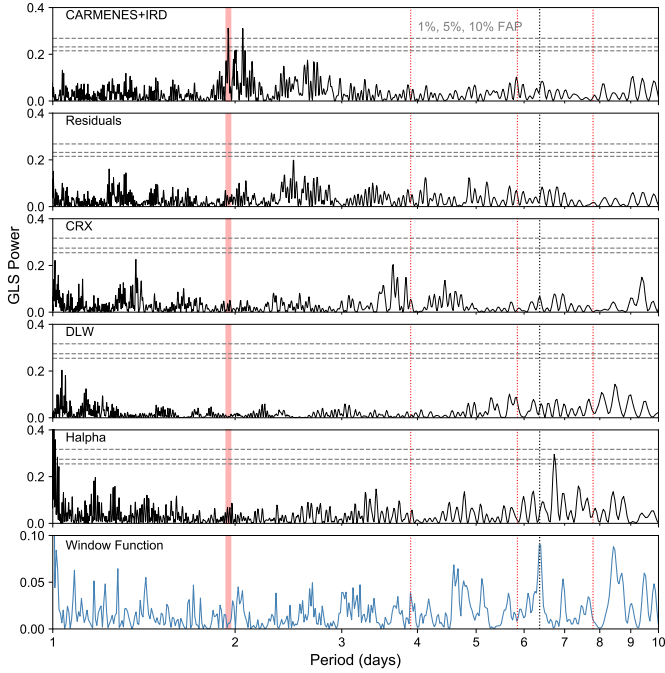


**Fig. 4.** GLS periodograms for the combined RVs, RV residuals from the fit, the activity indices CRX, dLW, and  $H\alpha$ , and the window function. The dotted horizontal lines represent the 1, 5, and 10% FAP. The red shaded area is the position of the orbital period of the planet, and the vertical dotted red lines are aliases of that period. The vertical dotted black line represents the 6.4 d stellar rotation period by [Newton et al. \(2016\)](#).

### 3. Analysis

#### 3.1. Stellar parameters

The stellar parameters for this target were estimated using the CARMENES VIS stacked stellar template produced by `serval`. The  $T_{\text{eff}}$ ,  $\log g$ , and iron abundance [Fe/H] were determined through spectral fitting with a grid of PHOENIX-SESAM models following [Pasegger et al. \(2019\)](#), using the upper limit  $v \sin i = 2.0 \text{ km s}^{-1}$  from [Reiners et al. \(2018\)](#) and [Marfil et al. \(in prep.\)](#), who did not detect any rotational velocity. The luminosity,  $L_{\star}$ , was estimated by integrating the spectral energy distribution with the photometric data used by [Cifuentes et al. \(2020\)](#). The stellar radius,  $R_{\star}$ , was determined via the Stefan–Boltzmann law, and the stellar mass  $M_{\star}$  via the mass-radius relation from [Schweitzer et al. \(2019\)](#). We estimated the overall activity level of the star from the pseudo-equivalent width of the  $H\alpha$  line after the subtraction of an inactive stellar template,  $\text{pEW}'(H\alpha)$ , following [Schöfer et al. \(2019\)](#). We obtained a value of  $+0.040 \pm 0.026 \text{ \AA}$ , which indicates that LHS 1478 is a fairly inactive star ([Jeffers et al. 2018](#); [Schöfer et al. 2019](#)).

The star has a rotational period of 6.4 d, as listed by [Newton et al. \(2016\)](#), but the detection is deemed inconclusive. We looked at the SAP (Simple Aperture Photometry; [Morris et al. 2020](#)) and PDC data from TESS and, after masking the transits and performing a Lomb-Scargle periodogram, we could not detect any signal with a period of 6.4 d. Therefore, we agreed with [Newton et al. \(2016\)](#) in that the signal is a non-detection and may not correspond to the real rotational period for this star.

Time series of three activity indicators were extracted from the spectra with `serval`: the chromatic index (CRX), differential line width (dLW), and  $H\alpha$  ([Zechmeister et al. 2018](#)). We found

**Table 1.** Stellar parameters of LHS 1478.

Parameter	Value	Reference
Name	LHS 1478	Luy79
Karmn	J02573+765	Cab16
TOI	1640	ExoFOP-TESS
TIC	396562848	Sta18
$\alpha$ (J2000)	02 57 17.51	<i>Gaia</i> EDR3
$\delta$ (J2000)	+76 33 13.0	<i>Gaia</i> EDR3
Sp. type	m3 V <sup>(a)</sup>	This work
$J$ [mag]	$9.615 \pm 0.026$	Skr06
$G$ [mag]	$12.2481 \pm 0.0028$	<i>Gaia</i> EDR3
$T$ [mag]	$11.0548 \pm 0.0073$	Sta19
$\varpi$ [mas]	$54.904 \pm 0.018$	<i>Gaia</i> EDR3
$d$ [pc]	$18.214 \pm 0.006$	<i>Gaia</i> EDR3
$T_{\text{eff}}$ [K]	$3381 \pm 54$	This work
$\log g$ [cgs]	$4.87 \pm 0.06$	This work
[Fe/H] [dex]	$-0.13 \pm 0.19$	This work
$M_{\star}$ [ $M_{\odot}$ ]	$0.236 \pm 0.012$	This work
$R_{\star}$ [ $R_{\odot}$ ]	$0.246 \pm 0.008$	This work
$\rho_{\star}$ [ $\text{g cm}^{-3}$ ] <sup>(b)</sup>	$22.2 \pm 2.5$	This work
$L_{\star}$ [ $10^{-4} L_{\odot}$ ]	$71.5 \pm 1.2$	Cif20
$\text{pEW}'(H\alpha)$ [ $\text{\AA}$ ]	$+0.040 \pm 0.026$	This work
$v \sin i$ [ $\text{km s}^{-1}$ ]	<2	Mar21
$P_{\text{rot}}$ [d]	[6.4] <sup>(c)</sup>	New16

**Notes.** <sup>(a)</sup>Spectral type estimated from photometry and parallax (with a lowercase “m”), as by [Cifuentes et al. \(2020\)](#). <sup>(b)</sup>Derived from  $M_{\star}$  and  $R_{\star}$ . <sup>(c)</sup>Flagged as a non-detection or an undetermined detection by [Newton et al. \(2016\)](#).

**References.** Luy79: [Luyten \(1979\)](#); Sta18: [Stassun et al. \(2018\)](#); Cab16: [Caballero et al. \(2016a\)](#); Skr06: [Skrutskie et al. \(2006\)](#); *Gaia* EDR3: [Gaia Collaboration \(2021\)](#); Sta19: [Stassun et al. \(2019\)](#); Cif20: [Cifuentes et al. \(2020\)](#); Mar21: [Marfil et al. \(in prep\)](#); New16: [Newton et al. \(2016\)](#).

no signs of periodic variations similar to the planet orbital period or the putative stellar rotational period of 6.4 d (Fig. 4). The only exception is for the  $H\alpha$  data, where there is a signal at  $\approx 6.8$  d with an FAP = 5%. This signal is not seen in any of the other indices or data sets, and, therefore, we could not provide any insight into its origin or relevance. The activity data are not correlated with the RV data either, with a correlation coefficient of  $|r| < 0.3$ . A summary of the stellar properties and relevant photometric and astrometric data from *Gaia* EDR3 is shown in Table 1.

#### 3.2. Joint fit

We used `juliet` ([Espinoza et al. 2019](#)) to perform a joint fit of the TESS, RCO, LCOGT, CARMENES, and IRD data. We used the efficient, uninformative sampling scheme from [Kipping \(2013\)](#) together with a quadratic law to parameterize the limb darkening in the TESS data. For the RCO and LCOGT data we used a linear limb-darkening law. We also followed the parameterization presented in [Espinoza \(2018\)](#), with parameters  $r_1$  and  $r_2$ , to fit for  $p$  and  $b$ , the planet-to-star radius ratio and impact parameter, respectively. The TESS data were fitted separately by sector, each with its own relative flux offset and jitter, but we imposed identical limb-darkening coefficients for the transit curves from all sectors. We fitted the LCOGT data separately for each observing night, but, as with the TESS data, we imposed an identical limb-darkening coefficient for the two

**Table 2.** Posterior distributions from the joint fit.

Parameter	Value
<i>Stellar density</i>	
$\rho_{\star}$ [ $\text{g cm}^{-3}$ ] <sup>(a)</sup>	$22.2^{+2.7}_{-2.3}$
<i>Orbital parameters</i>	
$P$ [d]	$1.9495378^{+0.0000040}_{-0.0000041}$
$T_0$ [BJD]	$2458786.75425^{+0.00042}_{-0.00042}$
$r_1$ <sup>(b)</sup>	$0.8111^{+0.0079}_{-0.0088}$
$r_2$ <sup>(b)</sup>	$0.0462^{+0.0011}_{-0.0010}$
$p = R_p/R_{\star}$	$0.0462^{+0.0011}_{-0.0010}$
$b = (a/R_{\star}) \cos i$	$0.717^{+0.012}_{-0.013}$
$i$ [deg]	$87.452^{+0.052}_{-0.048}$
$a/R_{\star}$	$16.119^{+0.088}_{-0.094}$
$K$ [ $\text{m s}^{-1}$ ]	$3.13^{+0.23}_{-0.25}$
$t_T$ [h]	$0.705^{+0.011}_{-0.011}$
<i>Derived planetary parameters</i>	
$M_p$ [ $M_{\oplus}$ ]	$2.33^{+0.20}_{-0.20}$
$R_p$ [ $R_{\oplus}$ ]	$1.242^{+0.051}_{-0.049}$
$\rho_p$ [ $\text{g cm}^{-3}$ ]	$6.67^{+1.03}_{-0.89}$
$a$ [au]	$0.01848^{+0.00061}_{-0.00063}$
$T_{\text{eq}}$ [K] <sup>(c)</sup>	$595^{+10}_{-10}$

**Notes.** The uncertainties represent the 68% CI of the obtained distributions. <sup>(a)</sup>Derived from light curve fitting using the relations from Seager & Mallén-Ornelas (2003). <sup>(b)</sup>Parameterization from Espinoza (2018) for  $p$  and  $b$ . <sup>(c)</sup>Assuming zero Bond albedo.

nights. The detrending of the TESS data was done by incorporating a Gaussian process (GP) model. We used the *celerite* Matérn kernel with a hyperparameter amplitude and the GP timescale given by  $\sigma_{\text{GP}}$  and  $\rho_{\text{GP}}$ , respectively (Foreman-Mackey et al. 2017). The same GP model was used for each TESS sector. An initial search for the optimal parameters of this system was done with *exostriker* (Trifonov 2019) using all data sets, and the results were used to build the priors for *juliet*, which are shown in Table A.3. The obtained posterior probabilities are listed in Tables 2 and A.4.

We built our full model, shown in Figs. 1 and 3, from the 68% confidence interval (CI) of the posterior distribution for each parameter. We found that the signal observed in both the photometric and RV data is consistent with a  $2.33^{+0.20}_{-0.20} M_{\oplus}$  and  $1.242^{+0.051}_{-0.049} R_{\oplus}$  planet, with a density of  $6.67^{+1.03}_{-0.89} \text{g cm}^{-3}$ , orbiting the star with a period of  $1.9495378^{+0.0000040}_{-0.0000041}$  d.

Since there is a brighter star ( $G \approx 10.30$  mag) about 120 arcsec north of LHS 1478, we checked for possible contamination in the TESS light curve. We analyzed the transit data from TESS and LCOGT, using the GP-detrended data, leaving the dilution factor as a free parameter for the TESS data, and fixing the limb-darkening coefficients to the values interpolated from limb darkening tables (Claret et al. 2013; Claret 2017). The parameters from Table 2 were recovered very well, and the best fit dilution factor is below 1% (and below 13% at 95% confidence). We conclude that the TESS light curve is therefore not contaminated.

A TLS search in the light curve residuals from the TESS data showed two significant periods at 13.9 and 27.8 d, but they were

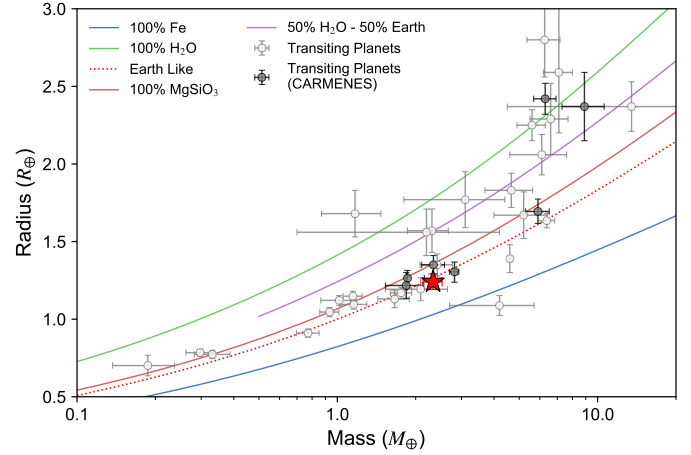


**Fig. 5.** Mass-radius diagram for LHS 1478 b (red star). The colored lines represent the composition models from Zeng et al. (2016, 2019). Transiting planets around M dwarfs with mass and radius measurements are shown in black circles (detected with CARMENES) and gray circles.

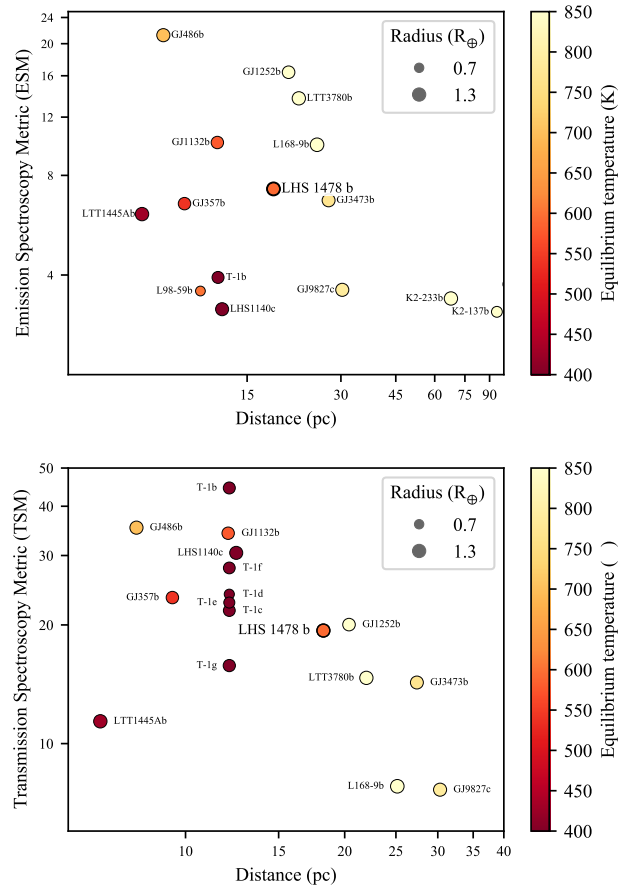


**Fig. 6.** ESM (top panel) and TSM (bottom panel) as a function of distance from the Sun for exoplanets with radii of less than  $1.5 R_{\oplus}$  and mass determinations by RVs or TTVs. LHS 1478 b is labeled and marked with a thicker black border in both panels.

due to the sampling of the data (Fig. A.3). A GLS periodogram of the residuals of the RV data did not show any significant signals either (Fig. 4). The obtained jitter terms for the RVs are within the expected instrumental jitter intervals for each instrument:  $\sim 1.2 \text{ m s}^{-1}$  for CARMENES VIS (Bauer et al. 2020) and  $\sim 2\text{--}3 \text{ m s}^{-1}$  for IRD (Hirano et al. 2020).

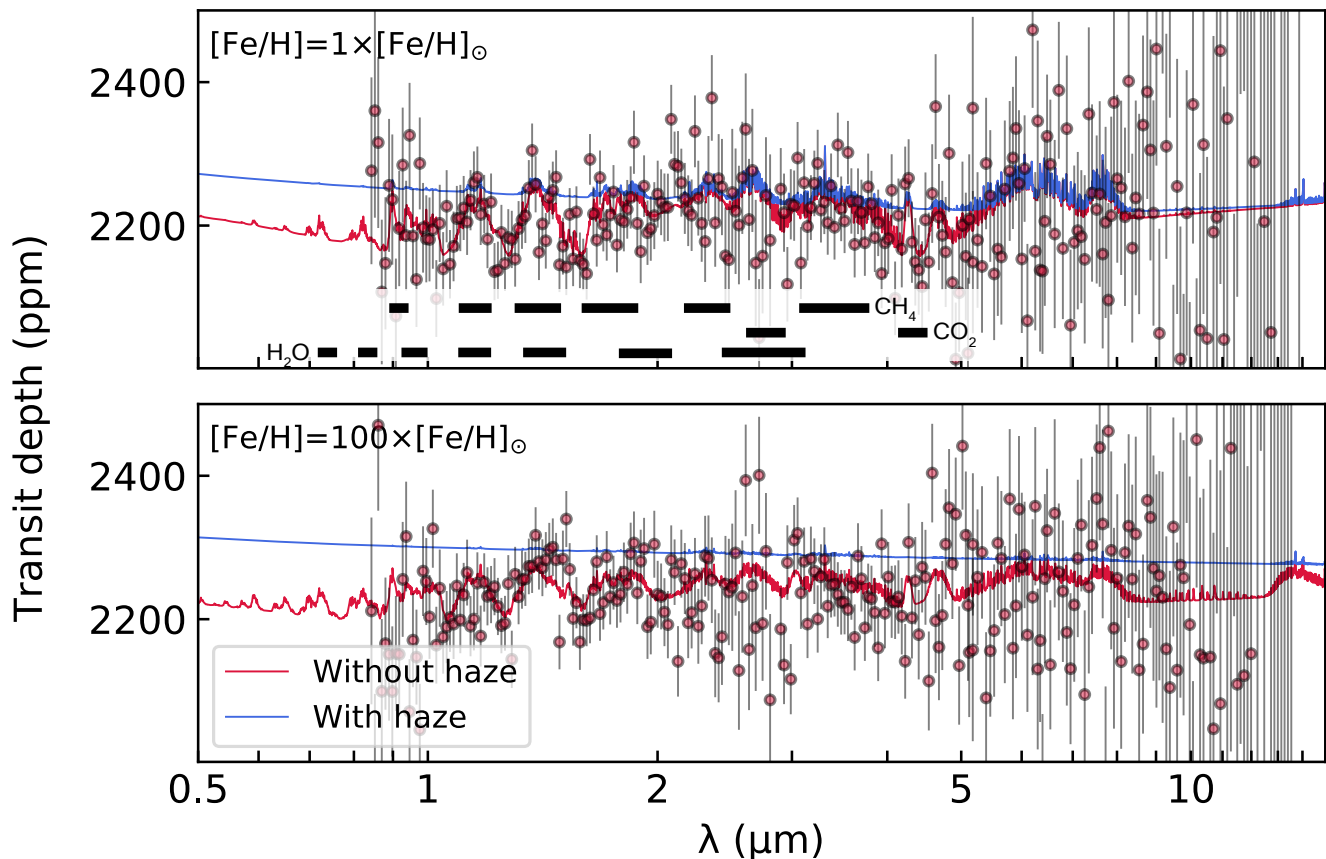


**Fig. 7.** Synthetic transmission atmospheric spectra of LHS 1478 b with haze opacity (solid blue lines) and without haze opacity (solid red lines). Simulated observations and estimated uncertainties are shown for the JWST NIRISS/SOSS (0.6–2.8  $\mu\text{m}$ ), NIRSpec/G395M (2.87–5.10  $\mu\text{m}$ ), and MIRI/LRS (5–12  $\mu\text{m}$ ) configurations, assuming two transits and binned for  $R = 50$  (filled circles with error bars). *Top*: fiducial models with solar abundance and the location of the strongest molecular features of  $\text{H}_2\text{O}$ ,  $\text{CH}_4$ , and  $\text{CO}_2$ . *Bottom*: metallicity enhanced by a factor of 100.

#### 4. Discussion and characterization prospects

Given the measured properties, we made a first exploratory guess of the planet composition. We compared its mass and radius with the models from Zeng et al. (2016, 2019), shown in Fig. 5, plus other transiting planets around M dwarfs from the literature<sup>8</sup>. We found that LHS 1478 b is compatible with a bulk composition of  $\sim 30\%$  Fe plus  $70\%$   $\text{MgSiO}_3$ . This makes its composition comparable to Earth’s, thus strongly supporting the notion that it is indeed a rocky world.

Atmospheric characterization of rocky planets with (some) properties similar to Earth’s is one of the pivotal developments expected in the forthcoming years thanks to the deployment of new ground- and space-based facilities. The potential of a target for detailed characterization is a complicated function of the planet and host star properties, as well as the instrument to be used. In this sense, not all transiting planets that have interesting properties are equally suitable for actual characterization.

As a first approximation of the suitability of LHS 1478 b, we calculated the spectroscopic metrics from Kempton et al. (2018), which were developed to rank the best TESS targets for the instrumentation aboard the *James Webb* Space Telescope (JWST). We estimated the emission spectroscopy metric (ESM) and the transmission spectroscopy metric (TSM) to be 7.28 and 19.35, respectively. The upper panel of Fig. 6 shows the ESMs of rocky exoplanets with measured masses, either through RVs

or transit timing variations (TTVs), and puts LHS 1478 b in that context. The ESM of 7.28 is slightly lower than the 7.5 threshold set by Kempton et al. (2018), but it is very close to that of Gl 1132 b, which was considered by the authors as a benchmark rocky planet for emission spectroscopy (after performing a recomputation of the ESM for Gl 1132 b, we found a value of 10.06, which is less than half of the ESM value of GJ 486 b, recently discovered by Trifonov et al. 2021). The lower panel illustrates TSM values. An acceptable TSM value for this class of planet is around 12 or higher (Table 1 in Kempton et al. 2018), which implies that LHS 1478 b is likely also an appropriate candidate for atmospheric characterization through transmission spectroscopy.

As a second refinement to its suitability for characterization, we assessed the potential chemical species that could be detected in its atmosphere using near-future instrumentation. Molecular features such as water, carbon dioxide, or methane should typically be observable on these kinds of planets if they maintain a substantial atmosphere (Molaverdikhani et al. 2019a,b), but the detectability of such features could also be obscured by the presence of clouds (Molaverdikhani et al. 2020). In order to quantitatively assess the potential of the atmospheric characterization observations of LHS 1478 b with the JWST, we calculated a few atmospheric models and their compositions using the photochemical code ChemKM (Molaverdikhani et al. 2019a) and their corresponding spectra using petitRADTRANS (Mollière et al. 2019). We assumed a stellar radiation environment similar to that measured for the well-studied star GJ 667C

<sup>8</sup> Data on transiting M dwarf planets at <https://carmenes.caha.es/ext/tmp/>

( $T_{\text{eff}} \approx 3327$  K). For the model of the planetary atmospheric structure, we adapted a Venus-like temperature profile to make it consistent with the derived equilibrium temperature of the planet (see Table 2). Our photochemical models included 135 species and 788 reactions.

Figure 7 shows simulated realizations of the transmission spectrum of LHS 1478 b, assuming solar metallicities (top panel) and 100-times-enhanced metallicities (bottom panel). The dominant spectral features come from water and methane, as expected, with a less extended CO<sub>2</sub> feature at around 4.5  $\mu\text{m}$ . The amplitudes of these features are between 50 and 100 ppm, which should be measurable given that the star is rather bright. This was verified using PandExo (Batalha et al. 2017) simulations of the NIRISS/SOSS, NIRSpec/G395M, and MIRI/LRS instruments and modes on board JWST.

Hydrogen-dominated atmospheres with temperatures below 900 K are expected to have significant photochemically produced hazes (e.g., He et al. 2018; Gao et al. 2020). If such a scenario applied to LHS 1478 b, it would result in the obscuration of spectral features, particularly in the case of an enhanced metallicity (see the bottom panel of Fig. 7). A relatively flat transmission spectrum thus might be indicative of a metallicity-enhanced atmosphere covered by haze, which might be indistinguishable from the planet having no atmosphere at all. If a (nearly) flat spectrum were observed, ground-based high-resolution spectroscopy could then be used to detect unobscured molecular features and break the associated degeneracies (see Brogi et al. 2017 and Gandhi et al. 2020 for more details on the possible features that could be detected).

In short, the simulations described in this section indicate that LHS 1478 b, along with GJ 357 b (Luque et al. 2019), GJ 1132 b (Berta-Thompson et al. 2015), and GJ 486 b (Trifonov et al. 2021), belongs to the small family of planets where we can realistically expect to obtain meaningful measurements and constraints with next-generation space telescopes such as JWST.

## 5. Conclusions

In this paper we present TESS and ground-based photometric observations, together with CARMENES and IRD Doppler spectroscopy, of the star LHS 1478. We determine LHS 1478 b to have a mass of  $2.33^{+0.20}_{-0.19} M_{\oplus}$ , a radius of  $1.242^{+0.050}_{-0.049} R_{\oplus}$ , and a bulk density of  $6.67^{+1.03}_{-0.89} \text{g cm}^{-3}$ , which is consistent with an Earth-like composition. The star is remarkably inactive, and we see no signs of additional planetary signals in the photometry or the RVs, which thus greatly simplifies the analysis.

The equilibrium temperature of this planet places it in a recently found group of warm rocky planets, together with GJ 357 b, GJ 1132 b, and GJ 486 b, which are ideal for atmospheric studies. The fact that the planetary signal is very isolated in both photometry and RV, with no stellar activity or additional companions contaminating it, together with the proximity of the system to the Sun and the relative brightness of the star make this an ideal target for near-future transit observations with JWST and ground-based high-resolution spectrometers.

*Acknowledgements.* CARMENES is an instrument at the Centro Astronómico Hispano-Alemán (CAHA) at Calar Alto (Almería, Spain), operated jointly by the Junta de Andalucía and the Instituto de Astrofísica de Andalucía (CSIC). CARMENES was funded by the Max-Planck-Gesellschaft (MPG), the Consejo Superior de Investigaciones Científicas (CSIC), the Ministerio de Economía y Competitividad (MINECO) and the European Regional Development Fund (ERDF) through projects FICTS-2011-02, ICTS-2017-07-CAHA-4, and CAHA16-CE-3978, and the members of the CARMENES Consortium

(Max-Planck-Institut für Astronomie, Instituto de Astrofísica de Andalucía, Landessternwarte Königstuhl, Institut de Ciències de l'Espai, Institut für Astrophysik Göttingen, Universidad Complutense de Madrid, Thüringer Landessternwarte Tautenburg, Instituto de Astrofísica de Canarias, Hamburger Sternwarte, Centro de Astrobiología and Centro Astronómico Hispano-Alemán), with additional contributions by the MINECO, the Deutsche Forschungsgemeinschaft through the Major Research Instrumentation Programme and Research Unit FOR2544 “Blue Planets around Red Stars”, the Klaus Tschira Stiftung, the states of Baden-Württemberg and Niedersachsen, and by the Junta de Andalucía. This paper included data collected by the TESS mission. Funding for the TESS mission is provided by the NASA’s Science Mission Directorate. Resources supporting this work were provided by the NASA High-End Computing (HEC) Program through the NASA Advanced Supercomputing (NAS) Division at Ames Research Center for the production of the SPOC data products. This work made use of observations from the LCOGT network. LCOGT telescope time was granted by NOIRLab through the Mid-Scale Innovations Program (MSIP), which is funded by the National Science Foundation. We acknowledge financial support from STFC grants ST/P000592/1 and ST/T000341/1, NASA grant NNX17AG24G, the Agencia Estatal de Investigación of the Ministerio de Ciencia, Innovación y Universidades and the ERDF through projects PID2019-109522GB-C5[1:4]/AEI/10.13039/501100011033, PGC2018-098153-B-C3[1,3] and the Centre of Excellence “Severo Ochoa” and “María de Maeztu” awards to the Instituto de Astrofísica de Canarias (SEV-2015-0548), Instituto de Astrofísica de Andalucía (SEV-2017-0709), and Centro de Astrobiología (MDM-2017-0737), the Generalitat de Catalunya/CERCA programme, Grant-in-Aid for JSPS Fellows Grant (JP20J21872), JSPS KAKENHI Grant (22000005, JP15H02063, JP18H01265, JP18H05439, JP18H05442, JP19K14783), JST PRESTO Grant (JPMJPR1775), and University Research Support Grant from the National Astronomical Observatory of Japan.

## References

- Aigrain, S., Parviainen, H., & Pope, B. J. S. 2016, *MNRAS*, 459, 2408  
 Aller, A., Lillo-Box, J., Jones, D., Miranda, L. F., & Barceló Fortera, S. 2020, *A&A*, 635, A128  
 Anglada-Escudé, G., Amado, P. J., Barnes, J., et al. 2016, *Nature*, 536, 437  
 Astudillo-Defru, N., Cloutier, R., Wang, S. X., et al. 2020, *A&A*, 636, A58  
 Batalha, N. E., Mandell, A., Pontoppidan, K., et al. 2017, *PASP*, 129, 064501  
 Bauer, F. F., Zechmeister, M., Kaminski, A., et al. 2020, *A&A*, 640, A50  
 Berta, Z. K., Irwin, J., Charbonneau, D., Burke, C. J., & Falco, E. E. 2012, *AJ*, 144, 145  
 Berta-Thompson, Z. K., Irwin, J., Charbonneau, D., et al. 2015, *Nature*, 527, 204  
 Bhatti, W., Bouma, L., Joshua, John, & Price-Whelan, A. 2020, <https://doi.org/10.5281/zenodo.3723832>  
 Bluhm, P., Luque, R., Espinoza, N., et al. 2020, *A&A*, 639, A132  
 Brogi, M., Line, M., Bean, J., Désert, J. M., & Schwarz, H. 2017, *ApJ*, 839, L2  
 Brown, T. M., Baliber, N., Bianco, F. B., et al. 2013, *PASP*, 125, 1031  
 Caballero, J. A., Cortés-Contreras, M., Alonso-Floriano, F. J., et al. 2016a, in 19th Cambridge Workshop on Cool Stars, Stellar Systems, and the Sun (CS19), 148  
 Caballero, J. A., Guàrdia, J., López del Fresno, M., et al. 2016b, *SPIE Conf. Ser.*, 9910, 99100E  
 Cifuentes, C., Caballero, J. A., Cortés-Contreras, M., et al. 2020, *A&A*, 642, A115  
 Claret, A. 2017, *A&A*, 600, A30  
 Claret, A., Hauschildt, P. H., & Witte, S. 2013, *A&A*, 552, A16  
 Collins, K. A., Kielkopf, J. F., Stassun, K. G., & Hessman, F. V. 2017, *AJ*, 153, 77  
 Dreizler, S., Crossfield, I. J. M., Kossakowski, D., et al. 2020, *A&A*, 644, A127  
 Espinoza, N. 2018, *RNAAS*, 2, 209  
 Espinoza, N., Kossakowski, D., & Brahm, R. 2019, *MNRAS*, 490, 2262  
 Foreman-Mackey, D., Agol, E., Ambikasaran, S., & Angus, R. 2017, *AJ*, 154, 220  
 Gaia Collaboration (Brown, A. G. A., et al.) 2021, *A&A*, 649, A1  
 Gan, T., Shporer, A., Livingston, J. H., et al. 2020, *AJ*, 159, 160  
 Gandhi, S., Brogi, M., & Webb, R. K. 2020, *MNRAS*, 498, 194  
 Gao, P., Thorngren, D. P., Lee, G. K., et al. 2020, *Nat. Astron.*, 1, 951  
 Gillon, M., Triaud, A. H. M. J., Demory, B.-O., et al. 2017, *Nature*, 542, 456  
 Girardi, L., Barbieri, M., Groenewegen, M. A. T., et al. 2012, *Astrophys. Space Sci. Proc.*, 26, 165  
 He, C., Hörst, S. M., Lewis, N. K., et al. 2018, *AJ*, 156, 38  
 Hippke, M., & Heller, R. 2019, *A&A*, 623, A39  
 Hirano, T., Kuzuhara, M., Kotani, T., et al. 2020, *PASJ*, 72, 93  
 Hornumuth, F., Brandner, W., Hippler, S., & Henning, T. 2008, *J. Phys. Conf. Ser.*, 131, 012051  
 Irwin, J., Irwin, M., Aigrain, S., et al. 2007, *MNRAS*, 375, 1449



- Jeffers, S. V., Schöfer, P., Lamert, A., et al. 2018, *A&A*, 614, A76
- Jenkins, J. M. 2002, *ApJ*, 575, 493
- Jenkins, J. M., Chandrasekaran, H., McCauliff, S. D., et al. 2010, *SPIE Conf. Ser.*, 7740, 77400D
- Jenkins, J. M., Twicken, J. D., McCauliff, S., et al. 2016, *SPIE Conf. Ser.*, 9913, 99133E
- Jensen, E. 2013, *Astrophys. Source Code Libr.*, [[record ascl:1306.007](#)]
- Kanodia, S., Cañas, C. I., Stefansson, G., et al. 2020, *ApJ*, 899, 29
- Kemmer, J., Stock, S., Kossakowski, D., et al. 2020, *A&A*, 642, A236
- Kempton, E. M. R., Bean, J. L., Louie, D. R., et al. 2018, *PASP*, 130, 114401
- Kipping, D. M. 2013, *MNRAS*, 435, 2152
- Kotani, T., Tamura, M., Nishikawa, J., et al. 2018, *Proc. SPIE*, 10702, 1070211
- Kovács, G., Zucker, S., & Mazeh, T. 2002, *A&A*, 391, 369
- Kuzuhara, M., Hirano, T., Kotani, T., et al. 2018, *Proc. SPIE*, 10702, 1070260
- Li, J., Tenenbaum, P., Twicken, J. D., et al. 2019, *PASP*, 131, 024506
- Lightcurve Collaboration (Cardoso, J. V. d. M., et al.) 2018, *Astrophysics Source Code Library* [[record ascl:1812.013](#)]
- Lillo-Box, J., Barrado, D., & Bouy, H. 2012, *A&A*, 546, A10
- Lillo-Box, J., Barrado, D., & Bouy, H. 2014, *A&A*, 566, A103
- Lindegren, L., Klioner, S. A., Hernández, J., et al. 2021, *A&A*, 649, A2
- Luque, R., Nowak, G., Pallé, E., et al. 2018, *A&A*, 620, A171
- Luque, R., Pallé, E., Kossakowski, D., et al. 2019, *A&A*, 628, A39
- Luyten, W. J. 1979, *LHS catalogue. A catalogue of stars with proper motions exceeding 0.5'' annually* (Minneapolis: University of Minnesota)
- McCully, C., Volgenau, N. H., Harbeck, D.-R., et al. 2018, *SPIE Conf. Ser.*, 10707, 107070K
- Molaverdikhani, K., Henning, T., & Mollière, P. 2019a, *ApJ*, 883, 194
- Molaverdikhani, K., Henning, T., & Mollière, P. 2019b, *ApJ*, 873, 32
- Molaverdikhani, K., Henning, T., & Mollière, P. 2020, *ApJ*, 899, 53
- Mollière, P., Wardenier, J., van Boekel, R., et al. 2019, *A&A*, 627, A67
- Morris, R. L., Twicken, J. D., Smith, J. C., et al. 2020, *Kepler Data Processing Handbook: Photometric Analysis*, Kepler Science Document KSCI-19081-003
- Newton, E. R., Irwin, J., Charbonneau, D., et al. 2016, *ApJ*, 821, 93
- Nowak, G., Luque, R., Parviainen, H., et al. 2020, *A&A*, 642, A173
- Passegger, V. M., Schweitzer, A., Shulyak, D., et al. 2019, *A&A*, 627, A161
- Quirrenbach, A., Amado, P. J., Caballero, J. A., et al. 2016, *SPIE Conf. Ser.*, 9908, 990812
- Rackham, B. V., Apai, D., & Giampapa, M. S. 2018, *ApJ*, 853, 122
- Reiners, A., Zechmeister, M., Caballero, J. A., et al. 2018, *A&A*, 612, A49
- Ricker, G. R., Winn, J. N., Vanderspek, R., et al. 2015, *JATIS*, 1, 014003
- Schöfer, P., Jeffers, S. V., Reiners, A., et al. 2019, *A&A*, 623, A44
- Schweitzer, A., Passegger, V. M., Cifuentes, C., et al. 2019, *A&A*, 625, A68
- Seager, S., & Mallén-Ornelas, G. 2003, *ApJ*, 585, 1038
- Skrutskie, M. F., Cutri, R. M., Stiening, R., et al. 2006, *AJ*, 131, 1163
- Smith, J. C., Stumpe, M. C., Van Cleve, J. E., et al. 2012, *PASP*, 124, 1000
- Stassun, K. G., Oelkers, R. J., Pepper, J., et al. 2018, *AJ*, 156, 102
- Stassun, K. G., Oelkers, R. J., Paegert, M., et al. 2019, *AJ*, 158, 138
- Stock, S., Nagel, E., Kemmer, J., et al. 2020, *A&A*, 643, A112
- Strehl, K. 1902, *Astron. Nachr.*, 158, 89
- Tal-Or, L., Trifonov, T., Zucker, S., Mazeh, T., & Zechmeister, M. 2019, *MNRAS*, 484, L8
- Tamura, M., Suto, H., Nishikawa, J., et al. 2012, *Proc. SPIE*, 8446, 84461T
- Trifonov, T. 2019, *Astrophysics Source Code Library* [[record ascl:1906.004](#)]
- Trifonov, T., Tal-Or, L., Zechmeister, M., et al. 2020, *A&A*, 636, A74
- Trifonov, T., Caballero, J. A., Morales, J. C., et al. 2021, *Science*, 371, 1038
- Twicken, J. D., Catanzarite, J. H., Clarke, B. D., et al. 2018, *PASP*, 130, 064502
- Zechmeister, M., & Kürster, M. 2009, *A&A*, 496, 577
- Zechmeister, M., Anglada-Escudé, G., & Reiners, A. 2014, *A&A*, 561, A59
- Zechmeister, M., Reiners, A., Amado, P. J., et al. 2018, *A&A*, 609, A12
- Zechmeister, M., Dreizler, S., Ribas, I., et al. 2019, *A&A*, 627, A49
- Zeng, L., Sasselov, D. D., & Jacobsen, S. B. 2016, *ApJ*, 819, 127
- Zeng, L., Jacobsen, S. B., Sasselov, D. D., et al. 2019, *PNAS*, 116, 9723
- <sup>2</sup> Institut de Ciències de l'Espai (ICE, CSIC), Campus UAB, Can Magrans s/n, 08193 Bellaterra, Spain
- <sup>3</sup> Institut d'Estudis Espacials de Catalunya (IEEC), 08034 Barcelona, Spain
- <sup>4</sup> Institut für Astrophysik, Georg-August-Universität, Friedrich-Hund-Platz 1, 37077 Göttingen, Germany
- <sup>5</sup> Landessternwarte, Zentrum für Astronomie der Universität Heidelberg, Königstuhl 12, 69117 Heidelberg, Germany
- <sup>6</sup> Max-Planck-Institut für Astronomie, Königstuhl 17, 69117 Heidelberg, Germany
- <sup>7</sup> Instituto de Astrofísica de Andalucía (IAA-CSIC), Glorieta de la Astronomía s/n, 18008 Granada, Spain
- <sup>8</sup> Centro de Astrobiología (CSIC-INTA), ESAC, Camino bajo del castillo s/n, 28692 Villanueva de la Cañada, Madrid, Spain
- <sup>9</sup> Instituto de Astrofísica de Canarias, 38205 La Laguna, Tenerife, Spain
- <sup>10</sup> Departamento de Astrofísica, Universidad de La Laguna, 38206 La Laguna, Tenerife, Spain
- <sup>11</sup> Space Telescope Science Institute, 3700 San Martin Drive, Baltimore, MD 21218, USA
- <sup>12</sup> Komaba Institute for Science, The University of Tokyo, 3-8-1 Komaba, Meguro, Tokyo 153-8902, Japan
- <sup>13</sup> Japan Science and Technology Agency, PRESTO, 3-8-1 Komaba, Meguro, Tokyo 153-8902, Japan
- <sup>14</sup> Astrobiology Center, 2-21-1 Osawa, Mitaka, Tokyo 181-8588, Japan
- <sup>15</sup> Department of Earth and Planetary Science, The University of Tokyo, Tokyo, Japan
- <sup>16</sup> National Astronomical Observatory of Japan, 2-21-1 Osawa, Mitaka, Tokyo 181-8588, Japan
- <sup>17</sup> SETI Institute, Mountain View, CA 94043, USA
- <sup>18</sup> NASA Ames Research Center, Moffett Field, CA 94035, USA
- <sup>19</sup> Center for Astrophysics | Harvard & Smithsonian, 60 Garden St, Cambridge, MA, 02138, USA
- <sup>20</sup> Grand Pra Observatory, Switzerland
- <sup>21</sup> Observatori Astronòmic Albanyà, Camí de Bassegoda S/N, Albanyà 17733, Girona, Spain
- <sup>22</sup> Subaru Telescope, 650 N. Aohoku Place, Hilo, HI 96720, USA
- <sup>23</sup> Thüringer Landessternwarte Tautenburg, Sternwarte 5, 07778 Tautenburg, Germany
- <sup>24</sup> Department of Physics & Astronomy, Swarthmore College, Swarthmore PA 19081, USA
- <sup>25</sup> Department of Astronomy, School of Science, The Graduate University for Advanced Studies (SOKENDAI), 2-21-1 Osawa, Mitaka, Tokyo, Japan
- <sup>26</sup> MIT Kavli Institute for Astrophysics and Space Research, Massachusetts Institute of Technology, Cambridge, MA 02139, USA
- <sup>27</sup> Departamento de Física de la Tierra y Astrofísica and IPARCOS-UCM (Instituto de Física de Partículas y del Cosmos de la UCM), Facultad de Ciencias Físicas, Universidad Complutense de Madrid, 28040, Madrid, Spain
- <sup>28</sup> Department of Astronomy, The University of Tokyo, 7-3-1 Hongo, Bunkyo-ku, Tokyo 113-0033, Japan
- <sup>29</sup> Centro Astronómico Hispano-Alemán, Observatorio de Calar Alto, 04550 Gérgal, Almería, Spain
- <sup>30</sup> Hamburger Sternwarte, Universität Hamburg, Gojenbergsweg 112, 21029 Hamburg, Germany
- <sup>31</sup> Homer L. Dodge Department of Physics and Astronomy, University of Oklahoma, 440 West Brooks Street, Norman, OK 73019, USA
- <sup>32</sup> Department of Earth, Atmospheric and Planetary Sciences, Massachusetts Institute of Technology, Cambridge, MA 02139, USA
- <sup>33</sup> NASA Goddard Space Flight Center, 8800 Greenbelt Rd, Greenbelt, MD 20771, USA
- <sup>34</sup> Hazelwood Observatory, Australia
- <sup>35</sup> Planetary Discoveries, Fredericksburg, VA 22405, USA

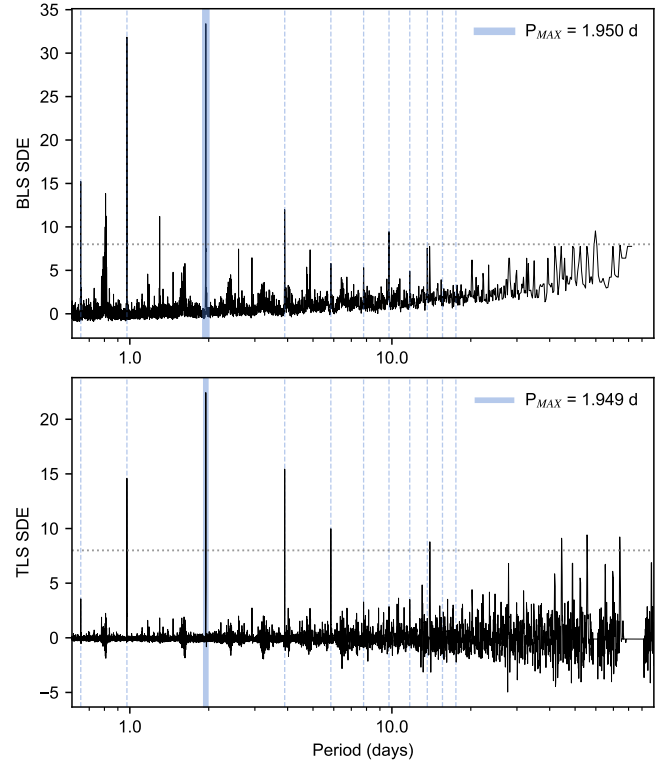
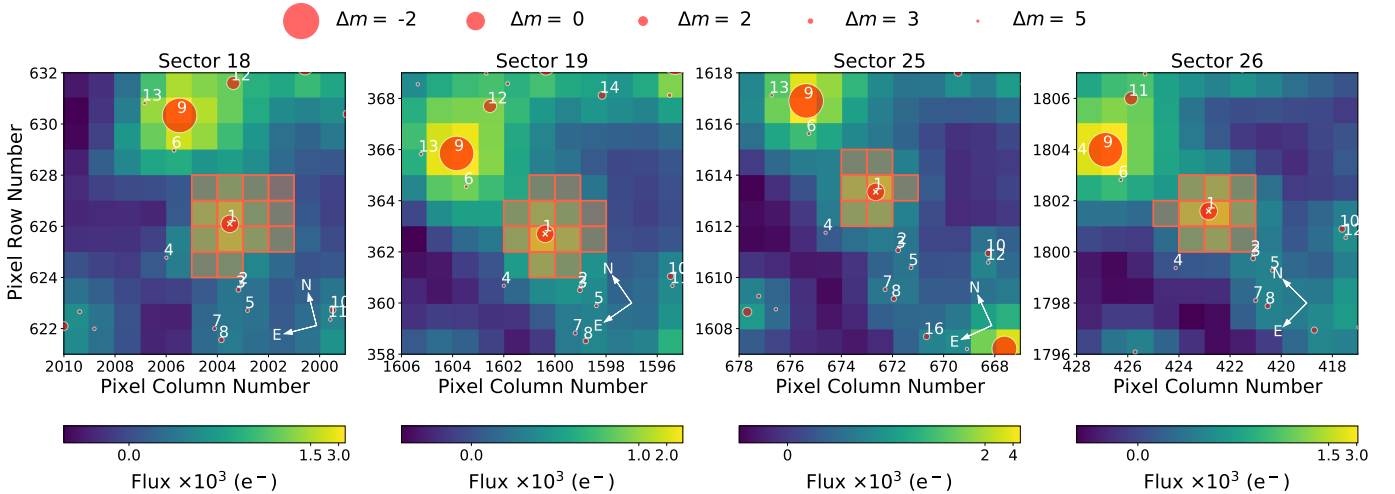
<sup>1</sup> School of Physics and Astronomy, Queen Mary University London, 327 Mile End Road, London E1 4NS, UK  
e-mail: maritsoto@ug.uchile.cl

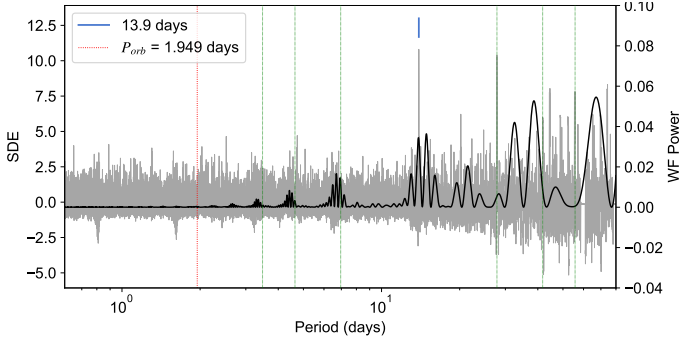
**Appendix A: Additional figures and tables****Table A.1.** RV data and activity indicators from CARMENES VIS.

BJD -2 450 000	RV (m s <sup>-1</sup> )	RV error (m s <sup>-1</sup> )	CRX (m s <sup>-1</sup> Np <sup>-1</sup> )	dLW (m <sup>2</sup> s <sup>-2</sup> )	H $\alpha$
8877.420	-4.54	2.03	11.0 $\pm$ 17.8	3.3 $\pm$ 2.4	0.934 $\pm$ 0.003
8881.348	1.71	2.40	2.0 $\pm$ 25.8	-20.4 $\pm$ 4.2	0.943 $\pm$ 0.004
8882.344	1.31	1.96	-8.3 $\pm$ 20.0	3.4 $\pm$ 1.8	0.930 $\pm$ 0.003
8883.412	-0.62	1.78	-8.0 $\pm$ 17.4	4.0 $\pm$ 1.9	0.925 $\pm$ 0.003
8884.348	-1.28	1.52	4.9 $\pm$ 14.8	8.2 $\pm$ 1.9	0.943 $\pm$ 0.003
8885.346	-0.87	2.33	-3.2 $\pm$ 23.4	9.3 $\pm$ 2.2	0.968 $\pm$ 0.004
8891.361	2.12	1.77	-1.9 $\pm$ 17.9	4.6 $\pm$ 1.6	0.949 $\pm$ 0.003
8893.372	-1.07	1.80	-22.7 $\pm$ 16.9	3.8 $\pm$ 1.9	0.923 $\pm$ 0.003
8894.345	-2.19	1.78	-15.2 $\pm$ 14.8	6.0 $\pm$ 1.8	0.930 $\pm$ 0.003
8895.364	2.81	2.54	-50.7 $\pm$ 25.3	-8.6 $\pm$ 2.1	0.925 $\pm$ 0.004
8896.368	-5.29	1.77	15.4 $\pm$ 18.2	-4.6 $\pm$ 2.1	0.933 $\pm$ 0.003
8897.353	-0.43	2.03	2.0 $\pm$ 21.8	-1.4 $\pm$ 1.9	0.928 $\pm$ 0.004
8904.361	-1.85	2.09	12.2 $\pm$ 18.9	-0.7 $\pm$ 2.0	0.937 $\pm$ 0.004
8913.365	0.36	2.24	-26.4 $\pm$ 22.9	0.9 $\pm$ 3.0	0.919 $\pm$ 0.004
8916.359	4.48	2.88	-58.1 $\pm$ 29.3	4.8 $\pm$ 4.0	0.920 $\pm$ 0.005
8918.371	-4.55	2.90	39.2 $\pm$ 30.7	43.1 $\pm$ 5.2	0.929 $\pm$ 0.005
8919.376	-0.22	3.00	13.4 $\pm$ 31.9	-9.4 $\pm$ 3.0	0.920 $\pm$ 0.005
8921.328	1.53	2.07	-0.6 $\pm$ 19.3	-4.8 $\pm$ 2.5	0.916 $\pm$ 0.003
8923.357	-2.78	1.92	8.2 $\pm$ 18.2	-2.6 $\pm$ 2.1	0.916 $\pm$ 0.003
9035.645	6.60	2.85	-43.2 $\pm$ 29.6	22.8 $\pm$ 4.5	0.917 $\pm$ 0.005
9036.639	-0.79	2.46	-32.8 $\pm$ 25.1	8.7 $\pm$ 2.4	0.907 $\pm$ 0.003
9037.633	2.53	2.19	12.1 $\pm$ 22.8	0.9 $\pm$ 1.8	0.920 $\pm$ 0.003
9047.655	-0.89	5.02	-28.1 $\pm$ 27.8	3.5 $\pm$ 2.2	0.908 $\pm$ 0.003
9049.595	1.42	2.35	17.0 $\pm$ 24.5	-7.1 $\pm$ 2.3	0.909 $\pm$ 0.004
9050.571	-2.27	2.19	-10.2 $\pm$ 19.9	-11.9 $\pm$ 2.7	0.901 $\pm$ 0.003
9051.580	3.27	4.09	-38.8 $\pm$ 41.5	-31.8 $\pm$ 5.5	0.922 $\pm$ 0.007
9054.590	-4.61	2.08	-50.6 $\pm$ 18.2	-0.5 $\pm$ 1.7	0.915 $\pm$ 0.003
9055.559	1.72	1.94	14.1 $\pm$ 18.3	-3.1 $\pm$ 2.3	0.912 $\pm$ 0.003
9056.575	0.94	2.48	5.6 $\pm$ 23.8	-7.8 $\pm$ 2.3	0.917 $\pm$ 0.004
9059.567	6.79	2.78	27.8 $\pm$ 28.9	-4.5 $\pm$ 2.4	0.932 $\pm$ 0.004
9060.656	1.85	2.67	18.2 $\pm$ 26.4	1.1 $\pm$ 2.9	0.924 $\pm$ 0.004
9061.554	6.87	2.28	-18.4 $\pm$ 22.1	4.3 $\pm$ 2.6	0.931 $\pm$ 0.004
9063.543	1.87	2.75	32.5 $\pm$ 29.1	10.0 $\pm$ 3.1	0.915 $\pm$ 0.005
9064.535	3.23	3.40	-18.5 $\pm$ 36.9	13.3 $\pm$ 3.6	0.920 $\pm$ 0.005
9111.691	4.61	3.54	47.2 $\pm$ 35.5	-4.9 $\pm$ 4.7	0.957 $\pm$ 0.007
9112.631	-5.92	2.46	25.0 $\pm$ 21.9	-1.8 $\pm$ 1.8	0.946 $\pm$ 0.004
9113.501	14.85	4.18	112.7 $\pm$ 42.5	-37.7 $\pm$ 6.8	0.947 $\pm$ 0.007
9114.403	3.22	3.41	67.2 $\pm$ 35.4	-22.7 $\pm$ 5.1	0.946 $\pm$ 0.005
9114.577	2.82	2.55	46.3 $\pm$ 24.7	-2.9 $\pm$ 2.3	0.939 $\pm$ 0.004
9115.595	4.73	3.93	94.9 $\pm$ 38.6	-1.9 $\pm$ 4.4	0.950 $\pm$ 0.006
9118.556	2.63	3.15	95.2 $\pm$ 27.2	-26.8 $\pm$ 5.0	0.947 $\pm$ 0.005
9119.480	5.98	2.49	10.0 $\pm$ 23.1	-4.0 $\pm$ 3.0	0.934 $\pm$ 0.004
9119.630	4.25	4.54	16.5 $\pm$ 49.0	-5.5 $\pm$ 4.7	0.947 $\pm$ 0.007
9120.495	-7.31	1.94	-2.1 $\pm$ 18.8	-0.6 $\pm$ 2.0	0.943 $\pm$ 0.003
9121.516	5.64	4.71	84.5 $\pm$ 49.1	48.3 $\pm$ 6.1	0.937 $\pm$ 0.008
9122.504	-5.05	2.59	42.6 $\pm$ 26.9	36.5 $\pm$ 4.1	0.935 $\pm$ 0.005
9122.662	-6.68	2.06	15.7 $\pm$ 21.2	-3.7 $\pm$ 2.8	0.920 $\pm$ 0.004
9126.500	-0.99	2.57	31.7 $\pm$ 24.1	1.2 $\pm$ 3.2	0.948 $\pm$ 0.005
9127.662	-1.77	3.39	64.7 $\pm$ 32.3	5.6 $\pm$ 3.2	0.943 $\pm$ 0.005
9128.527	-1.24	2.44	-32.1 $\pm$ 23.6	1.9 $\pm$ 1.7	0.941 $\pm$ 0.003
9128.644	-3.74	1.85	-5.5 $\pm$ 16.6	3.7 $\pm$ 1.7	0.931 $\pm$ 0.003
9132.594	-3.04	2.59	41.0 $\pm$ 24.1	-1.5 $\pm$ 2.4	0.918 $\pm$ 0.003
9132.694	0.97	3.56	64.1 $\pm$ 35.5	10.3 $\pm$ 3.5	0.905 $\pm$ 0.006
9138.394	-1.04	3.77	-69.0 $\pm$ 37.3	-0.1 $\pm$ 3.6	0.943 $\pm$ 0.006
9138.528	3.79	3.83	63.5 $\pm$ 38.4	-1.3 $\pm$ 4.2	0.930 $\pm$ 0.006
9138.595	5.45	3.38	-105.6 $\pm$ 30.0	-7.7 $\pm$ 4.0	0.915 $\pm$ 0.006
9138.672	3.15	4.22	-20.2 $\pm$ 44.0	-3.6 $\pm$ 3.5	0.913 $\pm$ 0.007

**Table A.2.** RV data from IRD.

BJD -2 450 000	RV (m s <sup>-1</sup> )	RV error (m s <sup>-1</sup> )
9120.014	-3.25	3.78
9120.024	-3.05	5.27
9123.071	-12.62	3.49
9123.082	-4.52	3.36
9152.992	10.43	5.03
9156.926	4.11	3.16
9157.012	-3.44	3.34
9188.842	6.78	6.78
9188.853	-0.39	5.99
9189.771	1.52	3.97
9189.781	-1.77	4.00
9189.890	4.69	3.60
9189.901	1.49	3.60


**Fig. A.1.** BLS (top panel) and TLS (bottom panel) SDE for the TESS light curve. The vertical blue lines correspond to aliases of the maximum period, highlighted by the blue shaded region. The dashed horizontal line at SDE = 8 in both panels corresponds to the threshold for transit detection from [Aigrain et al. \(2016\)](#).

**Fig. A.2.** TESS target pixel files for all four sectors that observed the target LHS 1478. The red shaded area corresponds to the apertures used to extract the photometry. The nearest sources to the target with up to 6 mag differences in the *Gaia* *G* passband are marked with red circles. The TESS pixel scale is  $\sim 21$  arcsec.



**Fig. A.3.** TLS of the TESS light curve residuals after subtracting the GP-plus-transit model. The dashed green lines are the aliases of the 13.9 d signal. The black line represents the window function of the data.

**Table A.3.** Priors used for the `juliet` run.

Parameter	Prior <sup>(a)</sup>
$M_{lc}^{(b)}$ [ppm]	$\mathcal{N}(0, 0.1)$
$\sigma_{lc}^{(b)}$ [ppm]	$\mathcal{LU}(0.1, 1000)$
$q_{1,TESS}$	$\mathcal{U}(0, 1)$
$q_{2,TESS}$	$\mathcal{U}(0, 1)$
$q_{1,LCO,RCO}$	$\mathcal{U}(0, 1)$
$\mu_{RV}$ [m s <sup>-1</sup> ] <sup>(c)</sup>	$\mathcal{N}(0, 0.2)$
$\sigma_{RV}$ [m s <sup>-1</sup> ] <sup>(c)</sup>	$\mathcal{LU}(10^{-4}, 15)$
$P$ [d]	$\mathcal{N}(1.949, 0.01)$
$T_0$ [BJD-2458000]	$\mathcal{N}(786, 0.01)$
$r_1$	$\mathcal{U}(0, 1)$
$r_2$	$\mathcal{U}(0, 1)$
$a/R_\star$	$\mathcal{N}(16.1, 0.2)$
$K$ [m s <sup>-1</sup> ]	$\mathcal{U}(0.2, 10)$
$e$	Fixed(0)
$\sigma_{GP,TESS}$ [ppm]	$\mathcal{LU}(10^{-6}, 10^6)$
$\rho_{GP,TESS}$ [d]	$\mathcal{LU}(10^{-3}, 10^3)$

**Notes.** <sup>(a)</sup> $\mathcal{N}$ : normal distribution,  $\mathcal{LU}$ : log-uniform distribution,  $\mathcal{U}$ : uniform distribution. <sup>(b)</sup>The same prior distributions were assumed for the photometric data, where “lc” stands for the light curves of TESS sectors 18, 19, 25, 26, the two nights of photometry from LCOGT, and RCO. <sup>(c)</sup>The same prior distributions were assumed for the RV data (CARMENES and IRD).

**Table A.4.** Posterior distributions for the instrumental parameters.

Parameter	Value
<i>Photometric parameters</i>	
$M_{S18}$ [10 <sup>-6</sup> ppm]	$3.97^{+57.05}_{-56.47}$
$\sigma_{S18}$ [ppm]	$1.78^{+11.24}_{-1.51}$
$M_{S19}$ [10 <sup>-6</sup> ppm]	$-16.15^{+52.67}_{-50.37}$
$\sigma_{S19}$ [ppm]	$1.99^{+12.69}_{-1.68}$
$M_{S25}$ [10 <sup>-6</sup> ppm]	$-75.50^{+51.51}_{-50.25}$
$\sigma_{S25}$ [ppm]	$2.04^{+13.31}_{-1.75}$
$M_{S26}$ [10 <sup>-6</sup> ppm]	$-12.42^{+53.02}_{-56.05}$
$\sigma_{S26}$ [ppm]	$1.91^{+11.40}_{-1.63}$
$M_{LCO1}$ [10 <sup>-6</sup> ppm]	$-115.66^{+104.37}_{-103.52}$
$\sigma_{LCO1}$ [ppm]	$977.77^{+16.31}_{-30.72}$
$M_{LCO2}$ [10 <sup>-6</sup> ppm]	$-69.46^{+125.09}_{-123.14}$
$\sigma_{LCO2}$ [ppm]	$856.87^{+90.00}_{-107.94}$
$M_{RCO}$ [10 <sup>-6</sup> ppm]	$10.19^{+144.64}_{-143.99}$
$\sigma_{RCO}$ [ppm]	$651.31^{+250.94}_{-641.52}$
$q_{1,TESS}^{(a)}$	$0.29^{+0.21}_{-0.16}$
$q_{2,TESS}^{(a)}$	$0.43^{+0.34}_{-0.29}$
$q_{1,LCO}$	$0.51^{+0.26}_{-0.28}$
$q_{1,RCO}$	$0.34^{+0.31}_{-0.23}$
<i>RV parameters</i>	
$\mu_{CARMENES}$ [m s <sup>-1</sup> ]	$0.04^{+0.17}_{-0.16}$
$\sigma_{CARMENES}$ [m s <sup>-1</sup> ]	$1.43^{+0.56}_{-0.70}$
$\mu_{IRD}$ [m s <sup>-1</sup> ]	$-0.26^{+0.43}_{-0.44}$
$\sigma_{IRD}$ [m s <sup>-1</sup> ]	$2.66^{+1.46}_{-1.91}$
<i>GP parameters</i>	
$GP_{\sigma,TESS}$ [10 <sup>-6</sup> ppm]	$339.76^{+20.12}_{-19.07}$
$GP_{\rho,TESS}$ [d]	$0.25^{+0.02}_{-0.02}$

**Notes.** The uncertainties represent the 68% CI of the obtained distributions. <sup>(a)</sup>Parameterization from [Kipping \(2013\)](#).